Calibrating sub-grid scale models for high-order wall-modeled large eddy simulation

Zhaowen Duan[1] and Z. J. Wang[2*]

*Correspondence:
zjw@ku.edu

[1] hiCFD, LLC, Lawrence 66049, Kansas, USA
[2] Department of Aerospace Engineering, The University of Kansas, Lawrence, KS 66045, USA

Abstract

High-order methods have demonstrated orders of magnitude reduction in computational cost for large eddy simulation (LES) over low-order methods in the past decade. Most such simulations are wall-resolved implicit LES (ILES) without an explicit sub-grid scale (SGS) model. The use of high-order ILES for severely under-resolved LES such as wall-modeled LES (WMLES) often runs into robustness and accuracy issues due to the low dissipation embedded in these methods. In the present study, we investigate the performance of several popular SGS models, the static Smagorinsky model, the wall-adapting local eddy-viscosity (WALE) model and the Vreman model, to improve the robustness and accuracy of under-resolved LES using high-order methods. The models are implemented in the high-order unstructured grid LES solver called hpMusic based on the discontinuous flux reconstruction method. The length scales in these SGS models are calibrated using the direct numerical simulation (DNS) database for the turbulent channel flow problem. The Vreman model has been found to produce the most accurate and consistent results with a proper choice of the length scale for WMLES.

Keywords: Sub-grid scale models, High-order methods, Wall-modeled large eddy simulation

1 Introduction

The promise offered by large eddy simulation (LES) to tackle complex turbulent flow problems is being realized in engineering applications five decades after its conception [1]. Wall-modeled LES has demonstrated its potential to accurately predict the maximum lift for the NASA high-lift Common Research Model (CRM-HL) from the 4th AIAA High-lift Prediction Workshop [2]. The cost and accuracy of LES lie between direct numerical simulation (DNS) and Reynolds-averaged Navier-Stokes (RANS) approaches since only the large eddies are resolved in LES while the effects of the small eddies are taken into account using sub-grid scale (SGS) models. The solution quality of LES is dictated by many factors including the resolution of the numerical methods, the computational mesh, the SGS model, the filter size, the quality of boundary conditions and wall models, etc. Overlooking any factor can lead to erroneous simulation results.
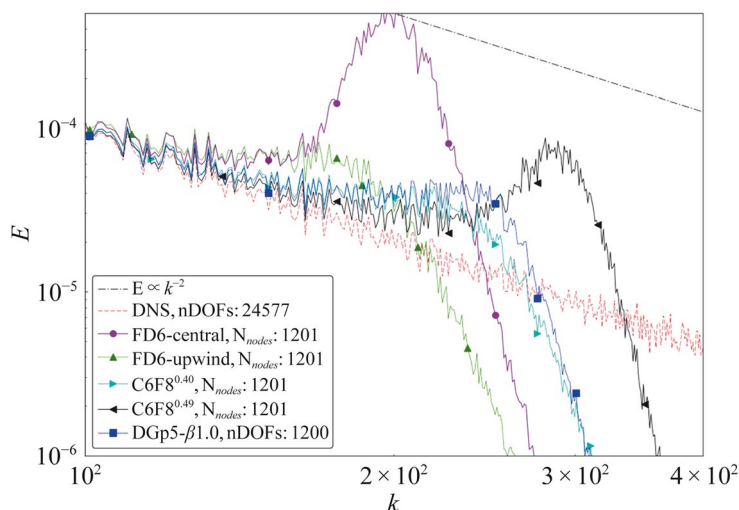
Fig. 1 Comparison of energy spectrum of various numerical schemes for the Burgers equation [10]

Even for the wind-tunnel scale CRM-HL, the cost of WMLES is very high and hundreds of millions of degrees-of-freedom (DOFs) are needed to obtain reasonable results with 2nd-order methods. The high cost continues to hinder the applications of LES in aerospace engineering because many problems have high Reynolds numbers well over 10 million. The development of high-order methods (3rd order and higher) [3–7] has reduced the cost of LES by orders of magnitude and pushed LES into the realm of design studies of mission-critical problems [8]. Because of the progress made in the past decade in numerical methods, mesh generation and high-performance CPU/GPU architectures, high-order wall-resolved LES (WRLES) can now be conducted for flow with a Reynolds number on the order of 1 million on medium-sized industrial-level computer clusters for turbo-machinery flow problems [9].

High-order methods have very low dissipation and dispersion errors. When they are used to solve non-linear conservation laws, one observes energy pile-up in high wave-number small scales. The degree of this pile-up depends on the dissipation and dispersion characteristics. In a comparative study of high-order central finite difference (FD), upwind biased FD, filtered compact difference (CD), and the discontinuous Galerkin (DG) methods [10], these schemes were tested to resolve a broadband spectrum with the Burgers equation. The filtered CD and DG methods have the highest resolution while the central FD has the lowest resolution because of the large dispersion error as shown in Fig. 1. The central FD scheme also produced the most energy pile-up in the high wave-number regime, which can cause an LES to crash due to negative pressure or density without other means to enhance stability. One can also see that all high-order schemes produced energy pile-ups of various degrees. For example, the (strongly) filtered CD and DG methods produced much smaller bumps in the energy spectrum. As a result, they have demonstrated excellent performance in WRLES of many complex turbulent flow problems because of the adequate resolution of the small near-wall scales [11–15].

However, for higher Reynolds number problems encountered in the aeronautical industry, WRLES will be too expensive for many years to come because of the excessive near-wall mesh resolution requirement [16, 17]. Although WRLES solves
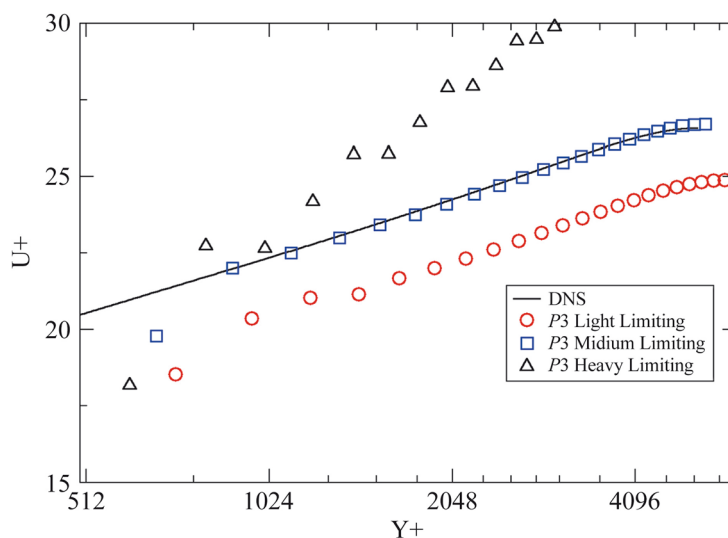
Fig. 2 Influence of solution limiting on the mean flow in a fully developed turbulent channel flow at $Re_\tau = 5200$ [34] computed using a 4th order discontinuous method

space-filtered Navier-Stokes equations and costs much less than DNS, the simulation expense is still very high because of the near-wall mesh resolution requirement [18]. WMLES [19], on the other hand, dramatically reduces the near-wall mesh resolution requirement and is much more affordable for real-world industrial applications [20–24].

In the near-wall region of WMLES, the turbulent scales are severely under-resolved. High-order ILES often encounters robustness and accuracy problems. The low dissipation embedded in high-order methods is often not sufficient to stabilize such simulations. Other means are usually necessary to achieve robust simulations such as solution limiting [25], filtering [26], polynomial dealiasing or over-integration [27–29], explicit SGS models [30–32], and various kinetic energy preserving (KEP) and entropy preserving (KEEP) schemes [33]. With such stabilizing techniques, the computations can proceed in a robust manner, but the accuracy often depends on how much small-scale energy is drained from the simulations. One such example is shown in Fig. 2, which illustrates the influence of solution limiting [25] on the mean flow in WMLES of the fully developed turbulent channel flow at a friction Reynolds number of 5,200. Note that insufficient damping of the small scales caused the wall friction to be over-predicted and the velocity to be under-predicted. On the other hand, the over-damping of the small scales caused the friction to be under-predicted and the velocity profile to be over-predicted. For complex configurations, it is very challenging to determine the appropriate amount of solution limiting. Filtering techniques also face this dilemma.

These challenges have led us to investigate the use of explicit SGS models in high-order WMLES. Early LES successes were largely attributed to the development of adequate SGS models, such as the classical Smagorinsky model [1], since they were critical in stabilizing very under-resolved LES. Various SGS models have been developed after the Smagorinsky model. The scale similarity model [35] assumes that the energy transfer between the resolved scales and unresolved scales is similar at different length scales.

The gradient model [36] estimates the local SGS stress tensor using a Taylor expansion of the flow velocity. The mixed model [37] combines the similarity model and the Smagorinsky model. To satisfy the physical condition of vanishing eddy viscosity near the wall, the wall-adapting local eddy-viscosity (WALE) model [38] and the Vreman model [39] were developed. The dynamic version of some of these models can be found in [40–45]. The development of SGS models for compressible flow is described in [46, 47]. A comprehensive review of SGS models is provided in [48].

SGS models and the underlying numerical methods are very tightly connected. For example, if a numerical method is non-dissipative, an adequate SGS model is essential for a stable and accurate LES. Otherwise, energy from the small subgrid scales is not drained and can pile up near the highest resolvable wave number to drive the simulation unstable. On the other hand, if a numerical scheme is dissipative, the energy from the small subgrid scales can often be sufficiently dissipated to main simulation stability without the use of an explicit SGS model for WMLES. For example, many high-resolution schemes with limiters have sufficient numerical dissipation to stabilize LES without a SGS model, thus popularizing the so-called implicit LES (ILES) [49]. Many studies also found that the use of SGS models in WRLES using high-order methods can be detrimental because of the excessive damping [50, 51]. This is because the SGS models introduced physically un-correlated dissipation and degraded the resolution of large eddies.

In the present study, we investigate several SGS models for under-resolved WMLES using the discontinuous flux reconstruction (FR) or correction procedure via reconstruction (CPR) method [7, 52–54]. More specifically, we study three popular SGS models, the Smagorinsky, WALE, and Vreman models, and calibrate the length scale for various solution polynomial orders using the DNS results of the channel flow. The present paper is organized as follows. Section 2 reviews the governing equations and the three SGS models. Section 3 describes the numerical method and the implementation of the SGS models in the FR/CPR method, followed by an introduction of the equilibrium wall model in Section 4. In Section 5, we compare the simulation results from the SGS models for several benchmark cases. Conclusions and future work are given in Section 6.

2 Governing equations and SGS models

2.1 Navier-Stokes equations for LES

The unsteady 3D Navier-Stokes equations governing the dynamics of compressible viscous flow can be written as [55]

$$\frac{\partial \rho}{\partial t} + \frac{\partial (\rho u_i)}{\partial x_i} = 0, \tag{1}$$

$$\frac{\partial (\rho u_i)}{\partial t} + \frac{\partial (\rho u_i u_j)}{\partial x_j} + \frac{\partial p}{\partial x_i} = \frac{\partial \tau_{ij}}{\partial x_j}, \tag{2}$$

$$\frac{\partial E}{\partial t} + \frac{\partial (E + p) u_j}{\partial x_j} = \frac{\partial (u_i \tau_{ij})}{\partial x_j} - \frac{\partial q_j}{\partial x_j}, \tag{3}$$

where ρ is the density, u_i are the velocity components, p is the pressure, E is the total energy, while τ_{ij} and q_j are the viscous stress tensor and heat flux. These are

$$\tau_{ij} = \mu \left(\frac{\partial u_i}{\partial x_j} + \frac{\partial u_j}{\partial x_i} \right) - \frac{2}{3} \mu \delta_{ij} \frac{\partial u_k}{\partial x_k}, \tag{4}$$

$$q_j = -\kappa \frac{\partial T}{\partial x_j}, \tag{5}$$

where μ is the viscosity, δ_{ij} is the Kronecker delta, T is the temperature and κ is the thermal conductivity, which is usually computed based on the Prandtl number Pr,

$$\kappa = \frac{c_p \mu}{Pr}, \tag{6}$$

with c_p the specific heat at constant pressure. The above equations use the summation convention for repeated indices. To close the equations, we employ the ideal gas law to compute the total energy,

$$E = \frac{p}{\gamma - 1} + \frac{1}{2} \rho u_i u_i, \tag{7}$$

where $\gamma = 1.4$ is the ratio of specific heats. For ILES, these equations can be directly used with the assumption that all variables are implicitly space-filtered quantities. The implicit filter width is related to the mesh size. For explicit LES, many terms need closure models to completely define the governing equations. For the sake of simplicity, we only augment the viscous stress tensor with a sub-grid stress term, i.e., $\tau_{ij} = \tau_{ij} + \tau_{ij}^{SGS}$. The SGS term is then computed with an SGS model. From a physical perspective, τ_{ij}^{SGS} accounts for the effect of the subgrid scales on the resolved scales. From a mathematical perspective, this is the extra term that appears in the filtered Navier-Stokes equations due to space filtering. While compressible flows also require modeling of the SGS pressure work, SGS heat transfer, SGS turbulent diffusion and SGS viscous diffusion, these additional terms are omitted for the low Mach number flows considered in the present study.

In the present study, three SGS models are studied in the context of the FR/CPR method. They are described next.

2.2 Smagorinsky model

The original SGS model introduced by Smagorinsky remains one of the most widely used eddy viscosity models which follows the Boussinesq hypothesis and set

$$\tau_{ij}^{SGS} = 2\rho \nu_{SGS} S_{ij}, \tag{8}$$

where ν_{SGS} is the eddy viscosity and S_{ij} is the rate of strain tensor,

$$S_{ij} \equiv \frac{1}{2} \left(\frac{\partial u_j}{\partial x_i} + \frac{\partial u_i}{\partial x_j} \right). \tag{9}$$

The eddy viscosity has the dimensions of length squared times the velocity gradient. The length scale is taken as $c_s \Delta$ with Δ the filter width while the velocity gradient is taken as the magnitude of the rate of strain tensor. So the eddy viscosity is

$$\nu_{SGS} = (c_s \Delta)^2 S, \tag{10}$$

and $S = \sqrt{2S_{ij}S_{ij}}$ represents a Galilean invariant estimation of velocity differences over length scales of order Δ. The Smagorinsky coefficient c_s was estimated to be 0.16 by Lilly [56] for isotropic turbulence.

2.3 Wall-adapting local eddy-viscosity (WALE) model

The WALE model is also an eddy viscosity model with a different eddy viscosity. Let the velocity gradient tensor be

$$g_{ij} \equiv \frac{\partial u_j}{\partial x_i}. \tag{11}$$

A traceless symmetric part of the square of the velocity gradient tensor is defined as

$$S_{ij}^d \equiv \frac{1}{2}(g_{ij}^2 + g_{ji}^2) - \frac{1}{3}\delta_{ij}g_{kk}^2, \tag{12}$$

where $g_{ij}^2 = g_{ik}g_{kj}$. The eddy viscosity is computed as

$$\nu_{SGS} = (c_w \Delta)^2 \frac{\left(S_{ij}^d S_{ij}^d\right)^{3/2}}{\left(S_{ij}S_{ij}\right)^{5/2} + \left(S_{ij}^d S_{ij}^d\right)^{5/4}}, \tag{13}$$

where the constant c_w is often estimated to be 0.325. One of the advantages of the WALE model over the Smagorinsky model is the eddy viscosity contains both the strain rate and rotation rate of the turbulent structure. The eddy viscosity of the Smagorinsky model only contains the strain rate. To see this, Eq. (12) can be written as

$$S_{ij}^d = S_{ik}S_{kj} + \Omega_{ik}\Omega_{kj} - \frac{1}{3}\delta_{ij}(S_{mn}S_{mn} - \Omega_{mn}\Omega_{mn}), \tag{14}$$

where $\Omega_{ij} = \frac{1}{2}\left(\frac{\partial u_j}{\partial x_i} - \frac{\partial u_i}{\partial x_j}\right)$ is the rotation rate tensor. Another advantage of the WALE model is that the eddy viscosity is reduced in the vicinity of the wall to produce the proper asymptotic behavior.

2.4 Vreman model

We simplify the model by assuming an isotropic filter width in all directions. The eddy viscosity of the Vreman model is computed as

$$\nu_{SGS} = (c_v \Delta)^2 \sqrt{\frac{B_\beta}{g_{ij}g_{ij}}}, \tag{15}$$

with $\beta_{ij} = g_{mi}g_{mj}$, $B_\beta = \beta_{11}\beta_{22} - \beta_{12}^2 + \beta_{11}\beta_{33} - \beta_{13}^2 + \beta_{22}\beta_{33} - \beta_{23}^2$. The coefficient c_v is related to the Smagorinsky coefficient by $c_v \approx \sqrt{2.5}c_s$. The Vreman model also has the proper near-wall behavior similar to the WALE model.

3 Numerical method

The FR/CPR method was originally developed by Huynh in 2007 for hyperbolic partial differential equations [52], and was then extended to hybrid unstructured meshes in [53, 54]. More recent work was reviewed in [7]. Let Q be the vector of conserved variables, F_j and $F_{v,j}$ represent the inviscid and viscous flux vectors in each coordinate direction. The conservation laws can be written as

$$\frac{\partial Q}{\partial t} + \frac{\partial F_j(Q)}{\partial x_j} = \frac{\partial F_{v,j}(Q, \nabla Q)}{\partial x_j}. \tag{16}$$

Assume that the computational domain is discretized into non-overlapping elements. Each physical element is transformed to a standard element with coordinates (ξ_1, ξ_2, ξ_3) by the transformation matrix,

$$K_{ij} = \frac{\partial x_i}{\partial \xi_j}, K_{ij}^{-1} = \frac{\partial \xi_i}{\partial x_j}, J = det(K). \tag{17}$$

Also define

$$W = JK^{-1}. \tag{18}$$

The elements of W are the cofactors of K, and in a finite volume discretization, they are just the areas of the computational cells projected in the Cartesian coordinate directions. If a face of the physical element is mapped to a face in the standard element defined by

$$h(\xi_1, \xi_2, \xi_3) = 0, \tag{19}$$

the surface metrics of this face can be computed according to

$$\mathbf{n}A = \frac{\nabla^\xi h \cdot W}{|\nabla^\xi h|}, \tag{20}$$

where $\mathbf{n}$ is the local unit face normal having components (n_1, n_2, n_3), A is the local area, ∇^ξ is the gradient operator in the computational domain. The normal inviscid and viscous fluxes are defined as

$$F^n = F_j n_j, \tag{21}$$

$$F_v^n = F_{v,j} n_j. \tag{22}$$

Inside element k, a set of points (usually Gauss quadrature points) is selected to construct a degree P solution polynomial Q_k using the Lagrange interpolation. These points are called solution points (*SPs*). Let $Q_{k,q}$ be the solution at *SP q* on element k. The local solution and the solutions at immediate face neighbors are used to compute a local gradient ∇Q_k. Then the inviscid and viscous fluxes are computed at the *SPs*, which are used to obtain flux polynomials, $\hat{F}_j(Q_k)$ and $\hat{F}_{v,j}(Q_k, \nabla Q_k)$, again using Lagrange interpolations. The FR/CPR formulation can be written as [54]

$$\frac{\partial Q_{k,q}}{\partial t} + \left[\frac{\partial \hat{F}_j(Q_k)}{\partial x_j}\right]_q - \left[\frac{\partial \hat{F}_{v,j}(Q_k, \nabla Q_k)}{\partial x_j}\right]_q + \frac{1}{J_{k,q}}\sum_f\sum_l \alpha_{q,f,l}([F^n]_{f,l} - [F_v^n]_{f,l})A_{f,l} = 0,$$

(23)

where index f denotes the faces of the element, and index l indicates the flux points (*FPs*) on the faces, which are usually the face Gauss quadrature points, $\alpha_{q,f,l}$ are the lifting coefficients only depending on the shape of the element, $[F^n]$ and $[F_v^n]$ are the normal inviscid and viscous flux jumps at each flux point. Although the solution is generally discontinuous across element interfaces, the normal inviscid and viscous fluxes must be continuous across element interfaces at the flux points to ensure conservation. This unique inviscid flux is computed with the Roe Riemann solver [57] and the unique viscous flux is computed with common solutions and gradients at the *FPs*. They are called the common fluxes, i.e. F_{com}^n and $F_{v,com}^n$. In the present study, the common face gradients are computed with the BR2 approach [58].

The normal flux jumps are the difference between the common fluxes and the interpolated normal fluxes at the flux points, i.e.,

$$[F^n]_{f,l} = F_{com,f,l}^n - \hat{F}_{f,l}^n,$$

(24)

$$[F_v^n]_{f,l} = F_{v,com,f,l}^n - \hat{F}_{v,f,l}^n.$$

(25)

In the FR/CPR method, projecting an arbitrary solution onto the piece-wise polynomial space can be considered a space-filtering operation. As a result, the FR/CPR method without any SGS model becomes ILES. Adding an SGS model to the FR/CPR scheme is then equivalent to adding extra dissipation flux terms to the original formulation. The variation of the velocity gradient at each SP generally leads to a non-uniform eddy viscosity inside an element. To make the SGS model less oscillatory, we use an element-wise constant eddy viscosity instead of the local eddy viscosity. The constant eddy viscosity is the averaged value over the element,

$$\nu_{SGS} = \frac{1}{V}\sum_q w_q \nu_{SGS,q},$$

(26)

where $\nu_{SGS,q}$ is the local eddy viscosity at *SP* q, V is the volume of the element, and w_q is the quadrature weight at the *SP*.

In the implementation of an SGS model within the FR/CPR framework, we could have treated the SGS stresses in the standard way. In this case, common fluxes are introduced in the momentum and energy equations, which are related to the SGS stresses. Since the SGS stresses are not well correlated with the physical SGS stresses [51], their primary purpose is to dissipate energy from the small turbulence scales. To guarantee the conservation and minimize data communication for parallel implementations, we artificially set the common fluxes of all the SGS stresses to be zero at all element interfaces, i.e.,

$$\left(\tau_{ij}^{SGS}\right)_{com} = 0.$$

(27)
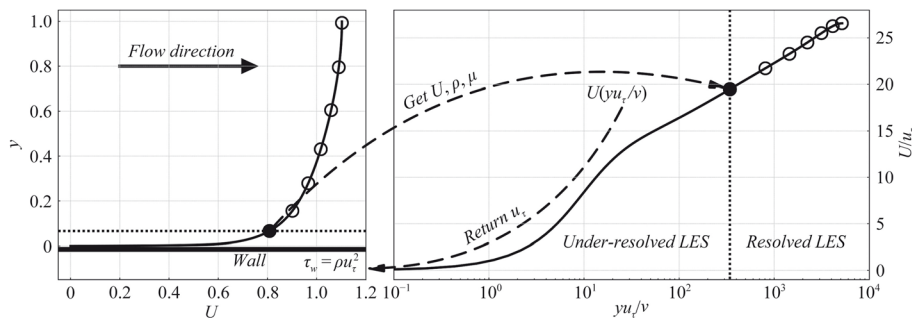
Fig. 3 Schematic of wall-modeled LES. The left figure depicts the boundary layer, while the right figure illustrates the law-of-the-wall [24]

In a *FV* method, each element has one degree of freedom (DOF). The filter width for all the SGS models is normally computed as

$$\Delta = V^{1/3}. \tag{28}$$

We will call this choice *d*1. In the FR/CPR method, there are multiple DOFs in an element. It seems that a natural choice for the filter width is then

$$\Delta = \frac{V^{1/3}}{P+1}. \tag{29}$$

We will call this choice *d*3. The SGS models have been mostly calibrated and used for 2nd-order methods. High-order methods have much less numerical dissipation than second-order ones. We thus expect choice *d*3 to not have sufficient dissipation for the small turbulence scales. We, therefore, introduce the following length scale between *d*1 and *d*3,

$$\Delta = \frac{V^{1/3}}{\sqrt{P+1}}, \tag{30}$$

which is called choice *d*2. Benchmark results will be used to assess the impact of these choices on the computational results.

For time integration, we employ either a 3rd order SSP Runge-Kutta scheme [59], or an optimized backward difference formula [60] with an LU-SGS solver [61, 62].

4 Equilibrium wall model

The equilibrium wall model used in the present study was developed in [24, 63], following an earlier attempt with an eddy-viscosity type model [64] and a wall model for the high-order DG method [65]. The basic idea is to obtain the wall model data from within the turbulent boundary layer. The distance from the data exchange location to the wall is denoted h_{wm}. Then the wall shear stress is computed based on the wall function, h_{wm}, and wall model data.

A schematic of the idea is shown in Fig. 3. The wall shear stress is obtained utilizing the law of the wall based on the wall parallel velocity input at a distance away from the wall,

where large eddies are captured. In Fig. 3, the dotted line separates the under-resolved inner region and the resolved outer region of the boundary layer. The black solid line is a sample DNS velocity profile in the boundary layer. The circles represent the solutions in the outer part of the boundary layer obtained using a resolved LES. The wall model takes the flow information including wall parallel velocity U, density ρ, and viscosity μ from the resolved LES as the input at the solid black circle in Fig. 3 and solves a nonlinear equation to obtain u_τ. Then the wall-stress $\tau_w = \rho u_\tau^2$ is imposed at the wall to update the solution unknowns near the wall.

In the present implementation of the high-order FR/CPR method, wall boundary conditions are imposed weakly at the wall flux points, as shown in Fig. 4. The data exchange location is on the interface between the first and second elements away from the wall. The wall model data are from the second element because the turbulent scales at the first element are always under-resolved. Since the near-wall eddy size is roughly the same as its distance to the wall, the desirable aspect ratio for the near-wall element is one because the eddy size at the second element is comparable to the element size. When the solution polynomial order P is sufficiently high, the turbulent eddies at the second element can be resolved well, thus providing accurate wall shear stress to update the degrees of freedom of the near-wall element.

5 Numerical results

5.1 Taylor-Green vortex evolution

The compressible inviscid Taylor-Green vortex problem [66] is chosen as the first case to assess the performance of the SGS models in stability and accuracy. In addition, we want to compare the dissipative characteristics of the SGS models relative to the Riemann solver. The spatial domain Ω is a box that spans $[-\pi L, \pi L]$ in each coordinate direction, and L is the characteristic length. The smooth initial conditions are given by the following equations.

$$\rho = \rho_0, \tag{31}$$

$$u = V_0 \sin\left(\frac{x}{L}\right) \cos\left(\frac{y}{L}\right) \cos\left(\frac{z}{L}\right), \tag{32}$$

$$v = -V_0 \cos\left(\frac{x}{L}\right) \sin\left(\frac{y}{L}\right) \cos\left(\frac{z}{L}\right), \tag{33}$$

$$w = 0, \tag{34}$$

$$p = p_0 + \frac{\rho_0 V_0^2}{16}\left(\cos\left(\frac{2x}{L}\right) + \cos\left(\frac{2y}{L}\right)\right)\left(\cos\left(\frac{2z}{L}\right) + 2\right), \tag{35}$$

where V_0 is the reference velocity, p_0 is the reference pressure, and ρ_0 is the reference density. The chosen reference state results in a Mach number $M_0 = 0.1$. The characteristic convective time is defined as $t_c = \frac{L}{V_0}$. The unsteady simulation is performed for $20t_c$ with an explicit 3rd order SSP Runge-Kutta scheme. It has been found in multiple
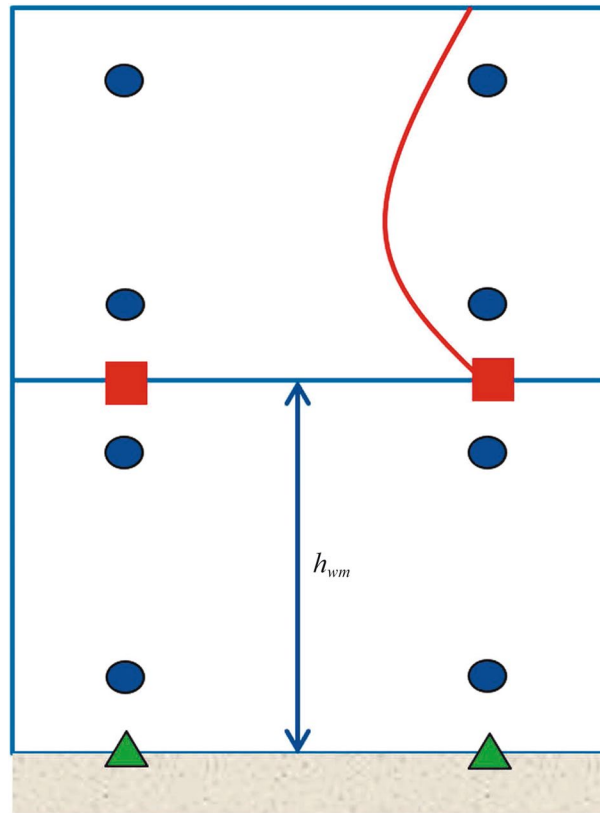
Fig. 4 Wall model implementation in the FR/CPR method. The green triangles denote the wall flux points, and the red squares denote the data exchange locations

international high-order CFD workshops that the kinetic energy and enstrophy are good resolution indicators for turbulent eddies. The non-dimensional kinetic energy is defined as

$$E_k = \frac{1}{\rho_0 V_0^2 \Omega} \int_\Omega \frac{1}{2} \rho \mathbf{v} \cdot \mathbf{v} d\Omega, \tag{36}$$

and the non-dimensional enstrophy is computed as

$$\chi = \frac{L^2}{\rho_0 V_0^2 \Omega} \int_\Omega \frac{1}{2} \rho \boldsymbol{\omega} \cdot \boldsymbol{\omega} d\Omega, \tag{37}$$

where $\mathbf{v}$ is the velocity vector, and $\boldsymbol{\omega} = \boldsymbol{\nabla} \times \mathbf{v}$ is the vorticity. To test the performance of the SGS models for under-resolved turbulence, the simulations were conducted assuming inviscid flow on a very coarse $16 \times 16 \times 16$ Cartesian grid at $P = 4$ ($P4$) with all the length scale choices for the SGS models. The kinetic energy and enstrophy histories are compared in Figs. 5 and 6. Both plots tell a similar story in the dissipative characteristics of the SGS models. It is striking that all three SGS models with any of the length scales heavily dissipated the turbulent eddies on this mesh compared to the ILES result. Both figures show that the amount of dissipation in the SGS models is much more than the dissipation embedded in high-order discontinuous methods due to the use of a Riemann
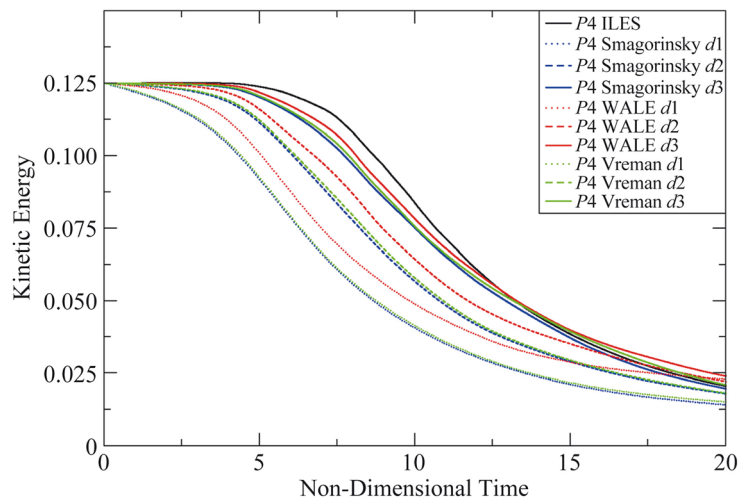
Fig. 5 Comparison of kinetic energy histories for the inviscid Taylor-Green vortex simulations at *P*4
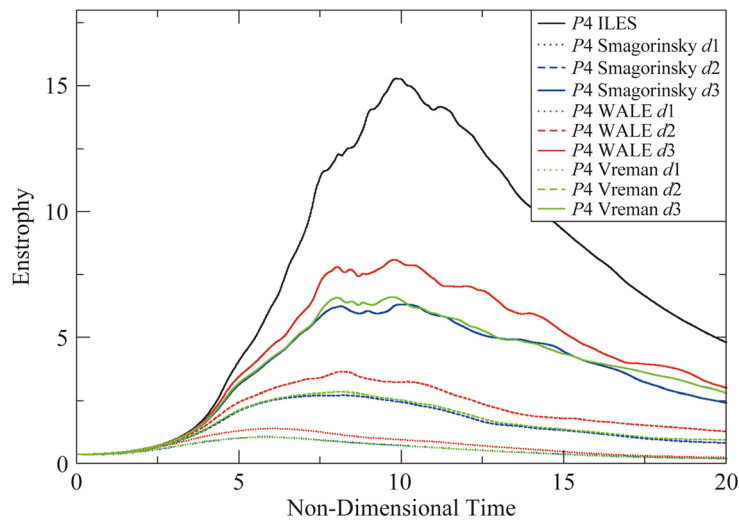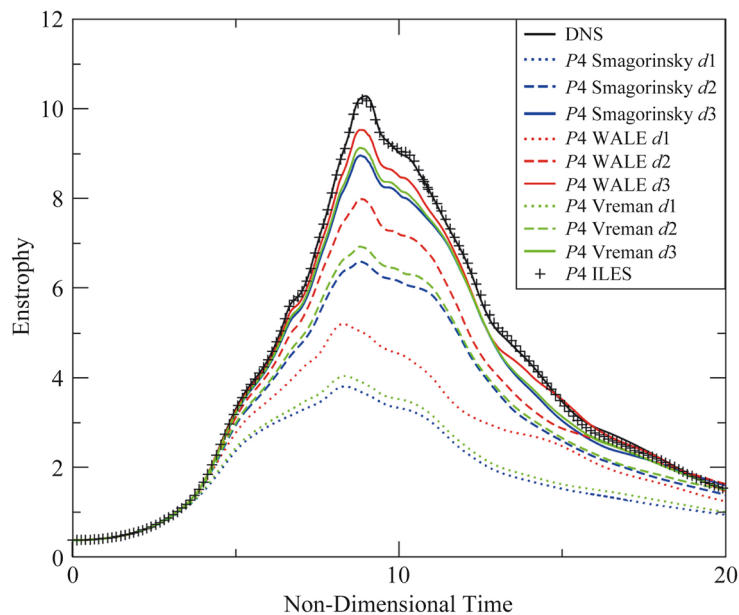

Fig. 6 Comparison of enstrophy histories for the inviscid Taylor-Green vortex simulations at *P*4

solver. In addition, the smaller dissipation with *d*2 and *d*3 is very obvious in comparison to the result with *d*1. Note that the WALE model is visibly less dissipative than either the Smagorinsy model or the Vreman model, while the Vreman model is slightly less dissipative than the Smagorinsky model.

Next, we test the performance of SGS models in a well-resolved simulation to see if and how they degrade the solution quality. A viscous simulation at

$$Re = \frac{\rho_0 V_0 L}{\mu} = 1,600 \tag{38}$$

was conducted on a mesh of 64^3 elements at *P*4. The Prandtl number is 0.71. The enstrophy histories from the present simulations are compared with the DNS results [66] in Fig. 7. The *P*4 *ILES* result is comparable to the DNS result at this resolution as their

Fig. 7 Comparison of enstrophy histories for the viscous Taylor-Green vortex simulations at *P*4

enstrophy histories are almost on top of each other. The SGS models appear to impact the enstrophy histories significantly with length scales of *d*1 and *d*2, and to a much less extent with *d*3. All three SGS models with *d*3 did not seriously degrade the results. Relatively speaking, we again confirm that the WALE model is the least dissipative, followed by the Vreman model while the Smagorinsky model is the most dissipative.

5.2 Isotropic turbulence

A decaying isotropic turbulence is simulated to study the impact of the SGS models on the kinetic energy spectra. We use the data collected by experiments of Comte-Bellot and Corrsin [67] for this purpose. In the experiments, the isotropic turbulence was triggered by a free-stream passing through a grid. Using the Taylor hypothesis, the spectra are measured at three downstream locations of the grid, which are converted into time instants of $U_0 t/M = 42$, 98, and 171, where $M = 5.08$ cm is the grid size and $U_0 = 10$ m/s is the free-stream velocity. The Reynolds number based on the grid size is $Re \equiv U_0 M/\nu = 34000$. In the present study, the isotropic turbulence is modeled inside a square box with periodic boundary conditions. The size of the box is chosen to be $L_B = 11M$. The initial random velocity field whose energy spectrum matches the experimental data at $U_0 t/M = 42$ is generated on a uniform Cartesian grid using the method proposed by Kwak et al. [68]. The random velocity field is then interpolated to the solution points of the computational mesh by tri-linear interpolations. The computational mesh is a Cartesian mesh with 32 cells in each direction. The computed turbulent kinetic energy spectra with different solution polynomial orders and SGS models are shown in Fig. 8 at $U_0 t/M = 98$. Note that the lower the solution polynomial order, the more energy pileup is observed near the high wave number regime compared to the experimental data. We believe this phenomenon was caused by the aliasing error due to a lack of resolution especially for $P = 2$ and $P = 3$. For $P = 4$ and $P = 5$, the spectra from the
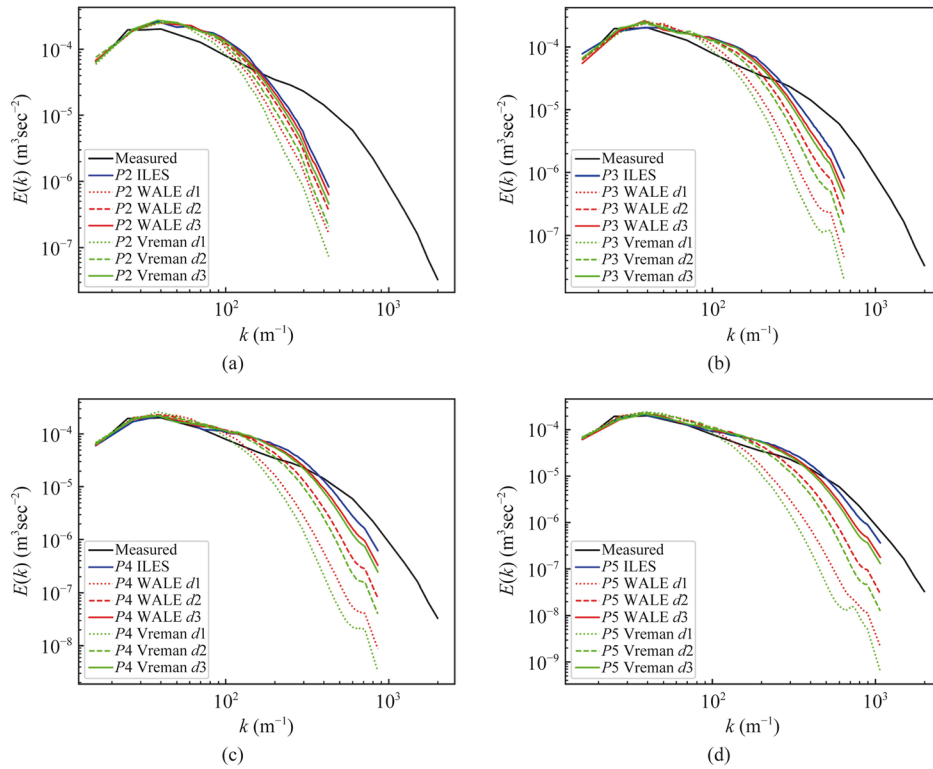
Fig. 8 Turbulent kinetic energy spectra at $U_0 t/M = 98$

simulations agree quite well with the measured spectra in the low wave number regime. It is obvious that the spectra of ILES simulations differ from the measured data the most in the high wave number regime compared to the spectra computed with the SGS models. One can also observe that both the WALE and Vreman models produced similar results, with the Vreman model having slightly more damping than the WALE model. This observation is compatible with the results in the Taylor-Green vortex case. The length scales in the SGS models caused a significant difference in damping characteristics, especially for $P = 4$ and $P = 5$. With length scale $d3$ (solid green and red curves), very little dissipation is introduced such that the energy spectra are very similar to the spectrum from the ILES simulations. On the other end, length scale $d1$ introduces too much dissipation that considerably reduces the range of resolvable wave numbers (dotted green and red curves). The SGS models with length scale $d2$ introduce a moderate amount of dissipation so that a good balance is achieved between resolution and energy dissipation near the highest resolvable wave numbers (dashed green and red curves).

5.3 Fully developed turbulent channel flow at $Re_\tau = 180$

This fully developed low Reynolds turbulent channel flow is selected to evaluate the performance of the SGS models for WRLES. The DNS data from [34] is used for comparison. The domain size is $[4\pi\delta, 2\delta, \frac{4}{3}\pi\delta]$, where δ is the half channel height. The Reynolds number based on δ and the friction velocity u_τ is $Re_\tau = \frac{u_\tau L}{\nu} = 180$. The bulk Mach number is 0.3. The grid has 100 elements in the stream-wise, 20 elements in the wall normal, and 33 elements in the spanwise directions respectively. The minimum element size in
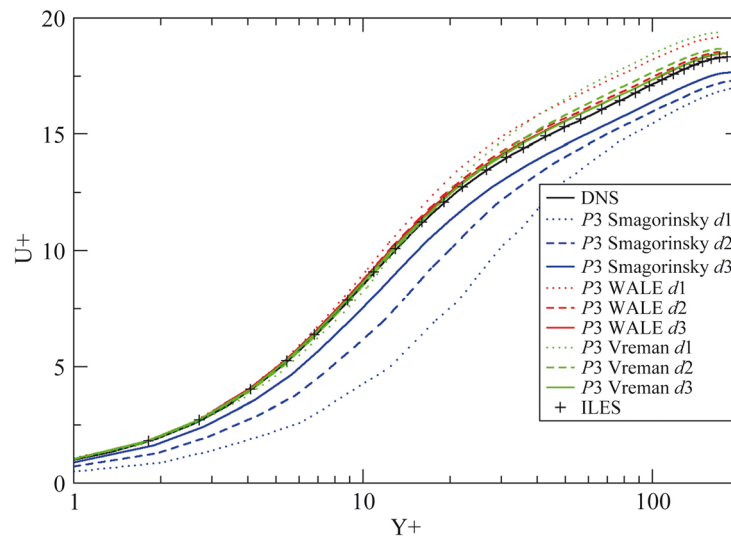
Fig. 9 Comparison of mean velocity profiles for the channel flow at $Re_\tau = 180$

the wall-normal direction is 0.015δ and the element growth rate is 1.5 in the wall normal direction. The flow variables are approximated with $P = 3$ polynomials resulting in an equivalent mesh resolutions of $\Delta x^+ = 5.7$, $\Delta y^+ = 0.68$, $\Delta z^+ = 5.7$. Periodic boundary conditions are applied in both the streamwise and spanwise directions. A source term is added dynamically to the x-momentum equation to maintain a constant bulk velocity through the channel. The temporal solver uses the block lower-upper symmetric Gauss-Seidel (LU-SGS) method [61, 62] together with a 2nd order optimized backward differential formula. The simulations were run sufficiently long to obtain converged mean flow and Reynolds stress profiles.

The mean velocity profiles computed with the SGS models at all length scales are compared with the DNS result and the ILES result in Fig. 9. Note first that the ILES result agrees very well with the DNS result because the present mesh resolution can be considered comparable to that of the DNS. It is obvious that the Smagorinsky model performed very poorly with all three length scales because of its large eddy viscosity near the wall boundary. This observation confirmed many earlier studies which showed that the Smagorinsky model degraded the accuracy of WRLES, e.g., [25]. The WALE and the Vreman models produced much better results than the Smagorinsky model, especially with lengths $d2$ and $d3$. Due to the proper near-wall behavior, both the WALE and Vreman models produced mean velocity profiles which agree very well with the DNS result in the viscous sublayer with $y^+ < 10$. With $d1$, both models performed poorly in the buffer and log regions. With $d2$ and $d3$, the mean velocity profiles agree much better with the DNS result in the entire boundary layer, with the WALE model performing slightly better than the Vreman model.

Next, we compare the computed Reynolds shear stress using the SGS models with the DNS result in Fig. 10. Again the Smagorinsky model did not perform well with any length scale. Both the WALE and Vreman models performed well with length scales $d2$ and $d3$, and the WALE model produced visibly better agreement with the DNS data than
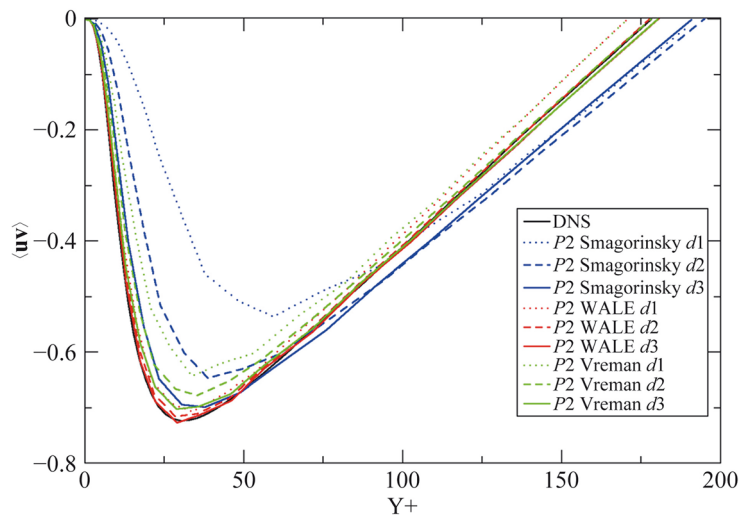
Fig. 10 Comparison of Reynolds shear stress profiles for the channel flow at $Re_\tau = 180$

the Vreman model. Obviously for this case, the smaller the eddy viscosity is, the better the agreement is with DNS because of the fine mesh resolution.

5.4 Fully developed turbulent channel flow at higher Reynolds numbers

The high Reynolds number channel flow problem at $Re_\tau = 5200$ is selected to evaluate the performance of the WALE and Vreman models for severely under-resolved turbulence with WMLES [63]. We again use the DNS data from [34] for comparison purposes. The computational domain is the same as the one used for the low Reynolds number case. A uniform grid was generated for WMLES with a total of $60 \times 16 \times 40$ elements. The mesh resolutions based on the element size in terms of wall units are roughly: $\Delta x^+ = 1088, \Delta y^+ = 650, \Delta z^+ = 544$.

At the present flow condition, ILES was not stable. Previously we used an accuracy-preserving limiter to stabilize the simulation. With the limiter, the computational results strongly depend on how much limiting is used as illustrated in Fig. 2. Therefore, the use of solution limiting for under-resolved turbulence becomes very ad hoc. Because of the poor performance of the Smagorinsky model for the low Reynolds number case, we only consider the WALE and Vreman models in the present simulations. In order to obtain a complete picture of the performance of both SGS models, $P2$ to $P5$ simulations were performed with all three length scales. The computed mean velocity profiles and Reynolds shear stresses are compared in Figs. 11, 12, 13, and 14.

Relatively speaking, the spread in the mean velocity profiles is larger than the spread in the Reynolds stress $\langle \mathbf{uv} \rangle$ for all solution orders. We therefore focus on comparing performance with the mean velocity profiles. At $P = 2$, both SGS models perform quite differently. With a decreasing length scale from $d1$ to $d3$, the mean velocity profiles shifted downward because of the reduced eddy viscosity. This trend is similar to that with a solution limiter. It is surprising, however, to see that the WALE model with the largest length scale $d1$ still failed to provide sufficient dissipation for the small turbulent scales in the case. Accordingly, the best result was produced with the
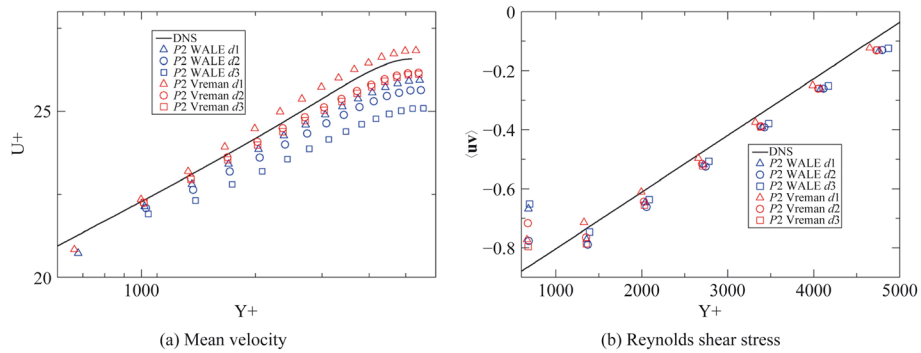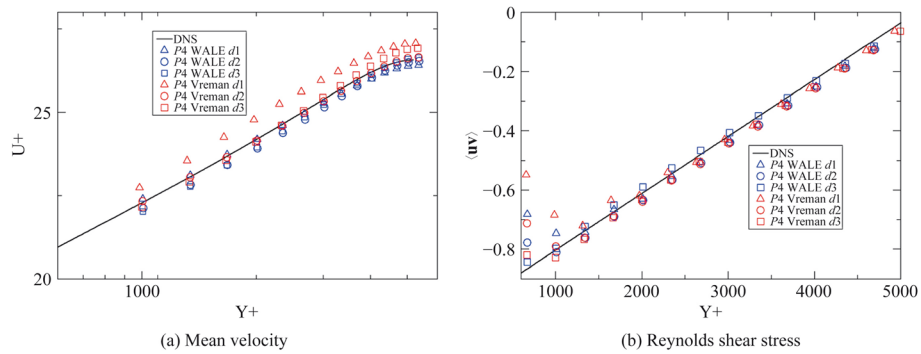
Fig. 11 Mean velocity and Reynolds stress (**uv**) computed with $P = 2$ at $Re_\tau = 5200$
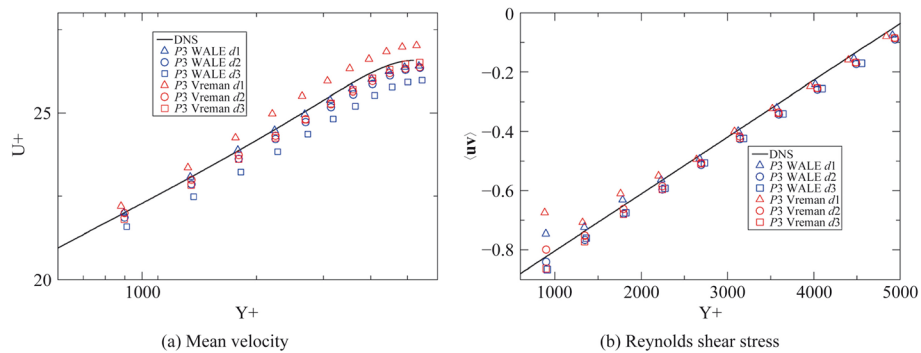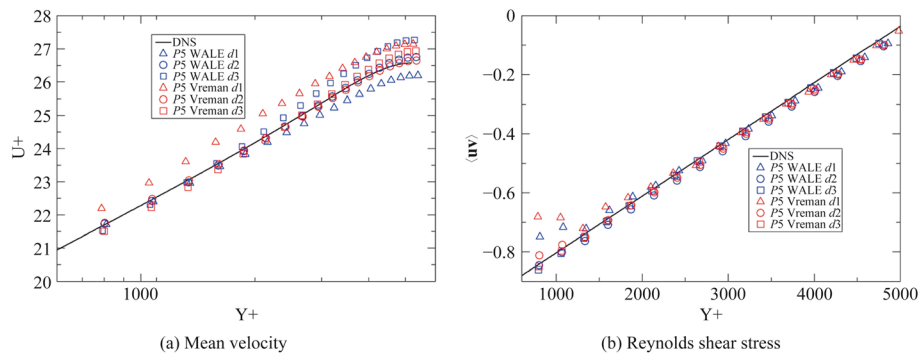

Fig. 12 Mean velocity and Reynolds stress (**uv**) computed with $P = 3$ at $Re_\tau = 5200$
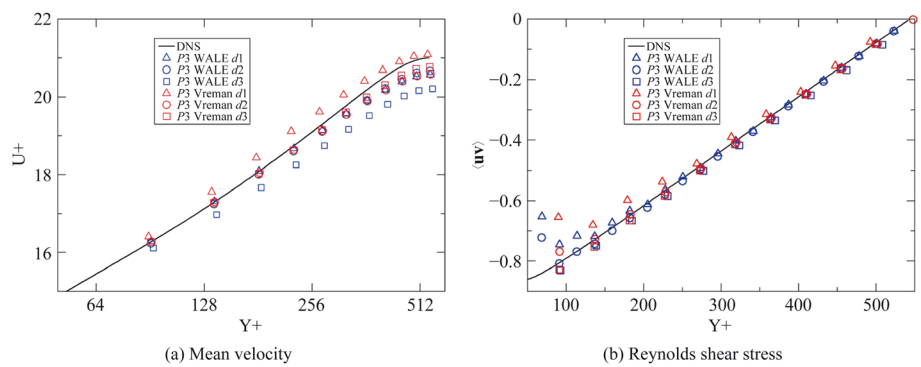

Fig. 13 Mean velocity and Reynolds stress (**uv**) computed with $P = 4$ at $Re_\tau = 5200$

largest length scale $d1$ for the WALE model. The Vreman model, on the other hand, performed as expected in that $d1$ has too much dissipation while $d3$ has too little dissipation with $d2$ generating the best agreement with the DNS data.

At $P = 3$ and $P = 4$, the velocity profiles computed with the WALE model agreed better with the DNS results at all length scales. The best result is still produced by the largest length scale $d1$. This trend, however, does not hold for $P = 5$. At $P = 5$, the best result is produced by $d2$ with the WALE model. It is strange to see that with a decreasing

(a) Mean velocity

(b) Reynolds shear stress

Fig. 14 Mean velocity and Reynolds stress $\langle \mathbf{uv} \rangle$ computed with $P = 5$ at $Re_\tau = 5200$

(a) Mean velocity

(b) Reynolds shear stress

Fig. 15 Mean velocity and Reynolds stress $\langle \mathbf{uv} \rangle$ computed with $P = 3$ at $Re_\tau = 544$

eddy viscosity from $d1$ to $d3$, the mean velocity profiles shifted upwards, completely reversing the trend observed from $P = 2$ to $P = 4$.

With the Vreman model, the results are very consistent in that $d1$ always has too much dissipation while $d3$ has too little dissipation with the best result produced by $d2$.

As a final verification of the performance evaluation, we perform a WMLES on the same mesh with $P = 3$ at the Reynolds number of $Re_\tau = 544$. The mesh resolutions based on the element size in terms of wall units are roughly: $\Delta x^+ = 114$, $\Delta y^+ = 68$, $\Delta z^+ = 57$. The computed mean velocity and Reynolds shear stress profiles are compared with the DNS results from [34] in Fig. 15. Even though this case has a Reynolds number nearly an order of magnitude smaller, the same performance trend is observed here: $d2$ produces the best results for the Vreman model and $d1$ generates the best result for the WALE model.

6 Conclusions

A comparative study of three SGS models, namely the Smagorinsky, the WALE and the Vreman models has been conducted in the present study for WRLES and WMLES with the discontinuous high-order FR/CPR method. These models have been used extensively in the CFD community and calibrated for second-order finite volume methods. Because of the vast difference in dissipative characteristics between second-order and high-order

methods, we expect that these SGS models need to be re-calibrated for high-order methods. Our decision is to retain the same model coefficient while revising the length scale in the SGS models. We therefore consider the following three length scales: $d1$: $\Delta = V^{1/3}$, $d2$: $\Delta = \frac{V^{1/3}}{\sqrt{P+1}}$, and $d3$: $\Delta = \frac{V^{1/3}}{P+1}$. Based on the benchmark problems of the Taylor-Green vortex, isentropic turbulence and the fully developed turbulent channel flows, we can draw the following conclusions:

- From the Taylor-Green vortex case, we can observe that SGS models introduce much more dissipation than the numerical dissipation embedded in the high-order discontinuous methods due to the use of Riemann solvers. The WALE model is the least dissipative, followed by the Vreman model, and the Smagorinsky model.
- The different length scales in the SGS models produced visibly different kinetic energy and enstrophy histories in the Taylor-Green vortex case for both under-resolved and well-resolved turbulence. Needless to say, ILES always performs the best for well-resolved turbulence.
- For the isentropic turbulence problem, both the WALE and the Vreman models performed similarly with the best results obtained with length scale $d2$.
- The channel flow case showed that the Smagorinsky model performed very poorly for wall-bounded flow due to its erroneous near-wall behavior. For WRLES, both the WALE and Vreman models performed reasonably well with length scales $d2$ and $d3$ while $d1$ produced large errors in the mean velocity profiles. We again confirmed conclusions from many studies which showed ILES performed better than explicit SGS models for WRLES.
- For WMLES, the most accurate and consistent results are delivered by the Vreman model from $P = 2$ to $P = 5$ with length scale $d2$. We therefore recommend the Vreman model for high-order WMLES with $d2$. In contrast, the WALE model's performance is not consistent with different solution polynomial orders. Even with the largest length scale $d1$, the WALE model appears to have insufficient dissipation to damp the small scales. At $P = 5$, the WALE model's behavior is unexpected. We therefore recommend the Vreman model for high-order WMLES with choice $d2$ as the length scale.

Authors' contributions
Zhaowen Duan: Methodology, Software, Simulation, Writing - Original draft. Z. J. Wang: Conceptualization, Methodology, Software, Simulation, Writing - Reviewing and Editing, Funding acquisition.

Availability of data and materials
The solution data will be available upon request.

Declarations

Competing interests
The authors do not have any competing interests.

References

1. Smagorinsky J (1963) General circulation experiments with the primitive equations. I. The basic experiment. Mon Weather Rev 91(3):99–164. https://doi.org/10.1175/1520-0493(1963)0912.3.CO;2
2. Kiris CC, Ghate AS, Browne OM et al (2022) HLPW-4/GMGW-3: Wall-modeled LES and lattice-Boltzmann technology focus group workshop summary. Paper presented at the AIAA aviation 2022 forum, Chicago, 27 June - 1 July 2022. https://doi.org/10.2514/6.2022-3294
3. Ekaterinaris JA (2005) High-order accurate, low numerical diffusion methods for aerodynamics. Prog Aerosp Sci 41(3–4):192–300. https://doi.org/10.1016/j.paerosci.2005.03.003
4. Wang ZJ (2007) High-order methods for the Euler and Navier–Stokes equations on unstructured grids. Prog Aerosp Sci 43(1–3):1–41. https://doi.org/10.1016/j.paerosci.2007.05.001
5. Vincent PE, Jameson A (2011) Facilitating the adoption of unstructured high-order methods amongst a wider community of fluid dynamicists. Math Model Nat Phenom 6(3):97–140. https://doi.org/10.1051/mmnp/20116305
6. Wang ZJ, Fidkowski K, Abgrall R et al (2013) High-order CFD methods: current status and perspective. Int J Numer Methods Fluids 72(8):811–845. https://doi.org/10.1002/fld.3767
7. Huynh HT, Wang ZJ, Vincent PE (2014) High-order methods for computational fluid dynamics: a brief review of compact differential formulations on unstructured grids. Comput Fluids 98:209–220. https://doi.org/10.1016/j.compfluid.2013.12.007
8. Bhaskaran R, Jia F, Laskowski GM et al (2017) Towards high-order large eddy simulation of aero-thermal flows for turbomachinery applications. In: Proceedings of the ASME turbo expo 2017: turbomachinery technical conference and exposition. Volume 2B: turbomachinery, Charlotte, 26-30 June 2017. https://doi.org/10.1115/GT2017-63358
9. Wang ZJ, Li Y, Jia F et al (2017) Towards industrial large eddy simulation using the FR/CPR method. Comput Fluids 156:579–589. https://doi.org/10.1016/j.compfluid.2017.04.026
10. Alhawwary M, Wang ZJ (2018) Fourier analysis and evaluation of DG, FD and compact difference methods for conservation laws. J Comput Phys 373:835–862. https://doi.org/10.1016/j.jcp.2018.07.018
11. Karamanos GS, Karniadakis GE (2000) A spectral vanishing viscosity method for large-eddy simulations. J Comput Phys 163(1):22–50. https://doi.org/10.1006/jcph.2000.6552
12. Visbal MR, Rizzetta DP (2002) Large-eddy simulation on curvilinear grids using compact differencing and filtering schemes. J Fluids Eng 124(4):836–847. https://doi.org/10.1115/1.1517564
13. Uranga A, Persson PO, Drela M et al (2011) Implicit large eddy simulation of transition to turbulence at low Reynolds numbers using a discontinuous Galerkin method. Int J Numer Methods Eng 87(1–5):232–261. https://doi.org/10.1002/nme.3036
14. Beck AD, Bolemann T, Flad D et al (2014) High-order discontinuous Galerkin spectral element methods for transitional and turbulent flow simulations. Int J Numer Methods Fluids 76(8):522–548. https://doi.org/10.1002/fld.3943
15. Vermeire BC, Nadarajah S, Tucker PG (2016) Implicit large eddy simulation using the high-order correction procedure via reconstruction scheme. Int J Numer Methods Fluids 82(5):231–260. https://doi.org/10.1002/fld.4214
16. Chapman DR (1979) Computational aerodynamics development and outlook. AIAA J 17(12):1293–1313. https://doi.org/10.2514/3.61311
17. Choi H, Moin P (2012) Grid-point requirements for large eddy simulation: Chapman's estimates revisited. Phys Fluids 24(1):011702. https://doi.org/10.1063/1.3676783
18. Alhawwary M, Wang ZJ (2019) On the mesh resolution of industrial LES based on the DNS of flow over the T106C turbine. Adv Aerodyn 1:21. https://doi.org/10.1186/s42774-019-0023-6
19. Deardorff JW (1970) A numerical study of three-dimensional turbulent channel flow at large Reynolds numbers. J Fluid Mech 41(2):453–480. https://doi.org/10.1017/S0022112070000691
20. Balaras E, Benocci C, Piomelli U (1996) Two-layer approximate boundary conditions for large-eddy simulations. AIAA J 34(6):1111–1119. https://doi.org/10.2514/3.13200
21. Cabot W, Moin P (2000) Approximate wall boundary conditions in the large-eddy simulation of high Reynolds number flow. Flow Turbul Combust 63:269–291. https://doi.org/10.1023/A:1009958917113
22. Larsson J, Kawai S, Bodart J et al (2015) Large eddy simulation with modeled wall-stress: recent progress and future directions. Mech Eng Rev 3(1):15–00418. https://doi.org/10.1299/mer.15-00418
23. Bose ST, Park GI (2018) Wall-modeled large-eddy simulation for complex turbulent flows. Ann Rev Fluid Mech 50(1):535–561. https://doi.org/10.1146/annurev-fluid-122316-045241
24. Shi J, Yan H, Wang ZJ (2020) Flux reconstruction implementation of an algebraic wall model for large-eddy simulation. AIAA J 58(7):3051–3062. https://doi.org/10.2514/1.J058957
25. Li Y, Wang ZJ (2017) A convergent and accuracy preserving limiter for the FR/CPR method. In: 55th AIAA aerospace sciences meeting, Grapevine, 9-13 January 2017. https://doi.org/10.2514/6.2017-0756
26. Fukushima Y, Haga T (2021) Assessment of wall-modeled LES with a flux-reconstruction method for high Reynolds number turbulent flows. Paper presented at the AIAA aviation 2021 forum, Virtual, 2-6 August 2021. https://doi.org/10.2514/6.2021-2750
27. Kirby RM, Karniadakis GE (2003) De-aliasing on non-uniform grids: algorithms and applications. J Comput Phys 191(1):249–264. https://doi.org/10.1016/S0021-9991(03)00314-0
28. Gassner GJ, Beck AD (2013) On the accuracy of high-order discretizations for underresolved turbulence simulations. Theor Comput Fluid Dyn 27:221–237. https://doi.org/10.1007/s00162-011-0253-7
29. Winters AR, Moura RC, Mengaldo G et al (2018) A comparative study on polynomial dealiasing and split form discontinuous Galerkin schemes for under-resolved turbulence computations. J Comput Phys 372:1–21. https://doi.org/10.1016/j.jcp.2018.06.016

30. Beck AD, Flad DG, Tonhäuser C et al (2016) On the influence of polynomial de-aliasing on subgrid scale models. Flow Turbul Combust 97:475–511. https://doi.org/10.1007/s10494-016-9704-y

31. Fernandez P, Nguyen NC, Peraire J (2017) Subgrid-scale modeling and implicit numerical dissipation in DG-based large-eddy simulation. In: 23rd AIAA computational fluid dynamics conference, Denver, 5-9 June 2017. https://doi.org/10.2514/6.2017-3951

32. Duan Z, Wang ZJ (2023) Comparative study of sub-grid scale models with high order flux reconstruction method for turbulent flows. Paper presented at the AIAA scitech 2023 forum, National Harbor, 23-27 January 2023. https://doi.org/10.2514/6.2023-1607

33. Flad D, Gassner G (2017) On the use of kinetic energy preserving DG-schemes for large eddy simulation. J Comput Phys 350:782–795. https://doi.org/10.1016/j.jcp.2017.09.004

34. Lee M, Moser RD (2015) Direct numerical simulation of turbulent channel flow up to $Re_\tau \approx 5200$. J Fluid Mech 774:395–415. https://doi.org/10.1017/jfm.2015.268

35. Bardina J, Ferziger JH, Reynolds WC (1980) Improved subgrid-scale models for large-eddy simulation. In: 13th fluid and plasma dynamics conference, Snowmass, 14-16 July 1980. https://doi.org/10.2514/6.1980-1357

36. Clark RA, Ferziger JH, Reynolds WC (1979) Evaluation of subgrid-scale models using an accurately simulated turbulent flow. J Fluid Mech 91(1):1–16. https://doi.org/10.1017/S002211207900001X

37. Zang Y, Street RL, Koseff JR (1993) A dynamic mixed subgrid-scale model and its application to turbulent recirculating flows. Phys Fluids A Fluid Dyn 5(12):3186–3196. https://doi.org/10.1063/1.858675

38. Nicoud F, Ducros F (1999) Subgrid-scale stress modelling based on the square of the velocity gradient tensor. Flow Turbul Combust 62(3):183–200. https://doi.org/10.1023/A:1009995426001

39. Vreman AW (2004) An eddy-viscosity subgrid-scale model for turbulent shear flow: Algebraic theory and applications. Phys Fluids 16(10):3670–3681. https://doi.org/10.1063/1.1785131

40. Germano M, Piomelli U, Moin P et al (1991) A dynamic subgrid-scale eddy viscosity model. Phys Fluids A Fluid Dyn 3(7):1760–1765. https://doi.org/10.1063/1.857955

41. Germano M (1992) Turbulence: the filtering approach. J Fluid Mech 238:325–336. https://doi.org/10.1017/S0022112092001733

42. Vreman B, Geurts B, Kuerten H (1996) Large-eddy simulation of the temporal mixing layer using the Clark model. Theor Comput Fluid Dyn 8(4):309–324. https://doi.org/10.1007/BF00639698

43. Morinishi Y, Vasilyev OV (2001) A recommended modification to the dynamic two-parameter mixed subgrid scale model for large eddy simulation of wall bounded turbulent flow. Phys Fluids 13(11):3400–3410. https://doi.org/10.1063/1.1404396

44. Yang Z, Cui G, Xu C et al (2012) Large eddy simulation of rotating turbulent channel flow with a new dynamic global-coefficient nonlinear subgrid stress model. J Turbul 13:N48. https://doi.org/10.1080/14685248.2012.726996

45. Ghaisas NS, Frankel SH (2016) Dynamic gradient models for the sub-grid scale stress tensor and scalar flux vector in large eddy simulation. J Turbul 17(1):30–50. https://doi.org/10.1080/14685248.2015.1083106

46. Pino Martín M, Piomelli U, Candler GV (2000) Subgrid-scale models for compressible large-eddy simulations. Theor Comput Fluid Dyn 13(5):361–376. https://doi.org/10.1007/PL00020896

47. Lenormand E, Sagaut P, Phuoc LT et al (2000) Subgrid-scale models for large-eddy simulations of compressible wall bounded flows. AIAA J 38(8):1340–1350. https://doi.org/10.2514/2.1133

48. Meneveau C, Katz J (2000) Scale-invariance and turbulence models for large-eddy simulation. Ann Rev Fluid Mech 32(1):1–32. https://doi.org/10.1146/annurev.fluid.32.1.1

49. Grinstein FF, Margolin LG, Rider WJ (2007) Implicit large eddy simulation: computing turbulent fluid dynamics. Cambridge University Press, Cambridge. https://doi.org/10.1017/CBO9780511618604

50. Garmann DJ, Visbal MR, Orkwis PD (2013) Comparative study of implicit and subgrid-scale model large-eddy simulation techniques for low-reynolds number airfoil applications. Int J Numer Methods Fluids 71(12):1546–1565. https://doi.org/10.1002/fld.3725

51. Li Y, Wang ZJ (2016) A priori and a posteriori evaluations of sub-grid scale models for the Burgers' equation. Comput Fluids 139:92–104. https://doi.org/10.1016/j.compfluid.2016.04.015

52. Huynh HT (2007) A flux reconstruction approach to high-order schemes including discontinuous Galerkin methods. In: 18th AIAA computational fluid dynamics conference, Miami, 25-28 June 2007. https://doi.org/10.2514/6.2007-4079

53. Wang ZJ, Gao H (2009) A unifying lifting collocation penalty formulation including the discontinuous Galerkin, spectral volume/difference methods for conservation laws on mixed grids. J Comput Phys 228(21):8161–8186. https://doi.org/10.1016/j.jcp.2009.07.036

54. Haga T, Gao H, Wang ZJ (2011) A high-order unifying discontinuous formulation for the Navier-Stokes equations on 3D mixed grids. Math Model Nat Phenom 6(3):28–56. https://doi.org/10.1051/mmnp/20116302

55. Jameson A (2022) Computational aerodynamics. Cambridge University Press, Cambridge. https://doi.org/10.1017/9781108943345

56. Lilly DK (1992) A proposed modification of the Germano subgrid-scale closure method. Phys Fluids A Fluid Dyn 4(3):633–635. https://doi.org/10.1063/1.858280

57. Roe PL (1981) Approximate Riemann solvers, parameter vectors, and difference schemes. J Comput Phys 43(2):357–372. https://doi.org/10.1016/0021-9991(81)90128-5

58. Bassi F, Rebay S (1997) A high-order accurate discontinuous finite element method for the numerical solution of the compressible Navier-Stokes equations. J Comput Phys 131(2):267–279. https://doi.org/10.1006/jcph.1996.5572

59. Gottlieb S, Shu CW, Tadmor E (2001) Strong stability-preserving high-order time discretization methods. SIAM Rev 43(1):89–112. https://doi.org/10.1137/S003614450036757X

60. Vatsa V, Carpenter M, Lockard D (2010) Re-evaluation of an optimized second order backward difference (BDF2OPT) scheme for unsteady flow applications. In: 48th AIAA aerospace sciences meeting including the new horizons forum and aerospace exposition, Orlando, 4-7 January 2010. https://doi.org/10.2514/6.2010-122

61. Jameson A, Yoon S (1987) Lower-upper implicit schemes with multiple grids for the Euler equations. AIAA J 25(7):929–935. https://doi.org/10.2514/3.9724

62. Chen RF, Wang ZJ (2000) Fast, block lower-upper symmetric Gauss-Seidel scheme for arbitrary grids. AIAA J 38(12):2238–2245. https://doi.org/10.2514/2.914
63. Wang ZJ (2022) High order wall-modeled large-eddy simulation on mixed unstructured meshes. AIAA J 60(12):6881–6896. https://doi.org/10.2514/1.J061641
64. Zhu H, Fu S, Shi L et al (2016) Implicit large-eddy simulation for the high-order flux reconstruction method. AIAA J 54(9):2721–2733. https://doi.org/10.2514/1.j054826
65. Frère A, Carton de Wiart C, Hillewaert K et al (2017) Application of wall models to discontinuous Galerkin LES. Phys Fluids 29(8):085111. https://doi.org/10.1063/1.4998977
66. van Rees WM, Leonard A, Pullin DI et al (2011) A comparison of vortex and pseudo-spectral methods for the simulation of periodic vortical flows at high Reynolds numbers. J Comput Phys 230(8):2794–2805. https://doi.org/10.1016/j.jcp.2010.11.031
67. Comte-Bellot G, Corrsin S (1971) Simple Eulerian time correlation of full- and narrow-band velocity signals in grid-generated, 'isotropic' turbulence. J Fluid Mech 48(2):273–337. https://doi.org/10.1017/S0022112071001599
68. Kwak D, Reynolds WC, Ferziger JH (1975) Three-dimensional time dependent computation of turbulent flow. NASA Contr Rep NASA-CR-166408

Publisher's Note